

# Classification of Microplastic Particles in Water using Polarized Light Scattering and Machine Learning Methods

## Authors

Leonard Saur<sup>1\*</sup>, Marc von Pawlowski<sup>1,2</sup>, Ulrich Gengenbach<sup>1</sup>, Ingo Sieber<sup>1</sup>, Hossein Shirali<sup>1</sup>, Lorenz Wührli<sup>1</sup>, Rainer Kiko<sup>3</sup>, Christian Pylatiuk<sup>1\*</sup>

- 1) Institute for Automation and Applied Informatics (IAI), Karlsruhe Institute of Technology (KIT), Hermann-von-Helmholtz-Platz 1, 76344 Eggenstein-Leopoldshafen, Germany
- 2) TÜV Süd Product Service GmbH, Ridlerstraße 65, 80339 München, Germany
- 3) GEOMAR Helmholtz Centre for Ocean Research Kiel, Wischhofstraße 1-3, 24148 Kiel, Germany

\* Corresponding authors: [leonard.saur@kit.edu](mailto:leonard.saur@kit.edu), [pylatiuk@kit.edu](mailto:pylatiuk@kit.edu)

## Abstract

Facing the critical need for continuous, large-scale microplastic monitoring, which is hindered by the limitations of gold-standard methods in aquatic environments, this paper introduces and validates a novel, reflection-based approach for the in-situ classification and identification of microplastics directly in water bodies, which is based on polarized light scattering. In this experiment, we classify colorless microplastic particles (50-300  $\mu\text{m}$ ) by illuminating them with linearly polarized laser light and capturing their reflected signals using a polarization-sensitive camera. This reflection-based technique successfully circumvents the transmission-based interference issues that plague many conventional methods when applied in water. Using a deep convolutional neural network (CNN) for image-based classification, we successfully identified three common polymer types, high-density polyethylene, low-density polyethylene, and polypropylene, achieving a peak mean classification accuracy of 80% on the test dataset. A subsequent feature hierarchy analysis demonstrated that the CNN's decision-making process relies mainly on the microstructural integrity and internal texture (polarization patterns) of the particle rather than its macroshape. Critically, we found that the Angle of Linear Polarization (AOLP) signal is significantly more robust against contextual noise than the Degree of Linear Polarization (DOLP) signal. While the AOLP-based classification achieved superior overall performance, its strength lies in distinguishing between the two polyethylene plastics, showing a lower confusion rate between high-density and low-density polyethylene. Conversely, the DOLP signal demonstrated slightly worse overall classification results but excels at accurately identifying the polypropylene class, which it isolated with greater success than AOLP.

## Keywords

Microplastics, Water research, Polarized light scattering, Stokes parameter, Machine learning

## 1. Introduction

Microplastics (MPs) are typically defined as plastic particles smaller than 5 mm, with lower size limits ranging from 1  $\mu$ m to 100 nm depending on the definition (Enfrin et al., 2021). They are recognized as one of the most pervasive classes of micro-pollutants and have been evidenced in marine, freshwater, and drinking water systems worldwide (Avio et al., 2017; Pivokonsky et al., 2018). MPs arise from two main sources: Primary microplastics that are intentionally manufactured, such as beads and fibers used in cosmetics and textile industries, and secondary microplastics formed by fragmentation of larger plastic materials through weathering factors including UV-light, fluctuating temperatures, biofouling, hydrolysis, and mechanical stress (Jahnke et al., 2017). Microplastics are ingested by a wide variety of aquatic organisms, raising concerns about trophic transfer and human exposure. Documented biological impacts include oxidative stress, inflammation, impaired organ function, and toxic responses to living cells, although the extent of risks to human health remains under debate (Rahman et al., 2021; Sharma and Chatterjee, 2017; Winiarska et al., 2024). These concerns highlight the need for reliable methods to monitor MPs in environmental waters. Current MP identification methods rely heavily on spectroscopic and thermal approaches. Fourier-transform infrared spectroscopy (FTIR) and Raman spectroscopy together account for the majority of analyses (Sesay et al., 2024; Shim et al., 2017; Veerasingam et al., 2021).

FTIR provides vibrational information from absorbed infrared light, but its application to aqueous samples is limited by the strong absorption of water (Al Alwan et al., 2024). Raman spectroscopy, which identifies materials based on inelastic light scattering that reveals molecular vibrational modes, overcomes this limitation but suffers from weak signal intensity, fluorescence interference, and potential heat-induced damage to particles. (Araujo et al., 2018; Jones et al., 2019; Schymanski et al., 2021). Pyrolysis–gas chromatography–mass spectrometry (Py-GC–MS) provides detailed polymer fingerprints but is destructive and complicated by organic matrices (Fischer and Scholz-Böttcher, 2019; Rauert et al., 2025). In contrast, sole visual microscopic inspections are widely used but show a strong observer dependence and labor intensity while not being able to distinguish polymer types from one another (Kotar et al., 2022; Lusher et al., 2020). Other techniques, such as ultrasound detection or chemical digestion, show potential but face challenges of sensitivity or secondary contamination (Sesay et al., 2024). These limitations have motivated the development of emerging approaches, including hyperspectral imaging (Beck et al., 2023), digital-holography (Huang et al., 2023; Zhu et al., 2024), and polarization-based scattering in combination with machine learning (Liu et al., 2021).

Polarization-sensitive methods utilize the interaction of light with microplastic particles, such as absorption, reflection, scattering, and refraction, which depend on size, shape, surface texture, and composition (Koestner et al., 2024, 2023). Recent studies have demonstrated that polarization features, combined with machine learning classifiers, can differentiate microplastics such as polystyrene from natural particles including algae (Liu et al., 2021) and discriminate multiple polymer types including polymethyl methacrylate (PMMA), polyethylene terephthalate glycol (PETG), polystyrene (PS), polyvinyl chloride (PVC), and polypropylene (PP) (Huang et al., 2023; Koestner et al., 2024; Zhu et al., 2024). Most of these approaches, however, rely on transmission geometries, which require transparent or semi-transparent samples and are therefore limited in realistic monitoring scenarios, such as turbid waters or opaque substrates (Mutuku et al., 2024; Zhu et al., 2024).

To address this gap, the present study explores a reflection-based polarization imaging method capable of distinguishing between morphologically similar and visually indistinct polymers (PP, high-density polyethylene (HDPE), low density polyethylene (LDPE)). In addition to enabling analysis under more practical conditions, this approach allows capture of particle size, shape, and color, providing traceability and opportunities for data reuse. By combining polarization-sensitive imaging with

convolutional neural networks (CNNs), we propose a new framework for fine-grained polymer classification with potential applications in remote detection and automated sorting in diverse aquatic environments.

## 2. Methods

### 2.1. Microplastic sample preparation

Non-additivated industrial plastic granules of PP, HDPE, and LDPE are obtained commercially (from LyondellBasell) and mechanically reduced in size using an abrasive tool under continuous water cooling to prevent heat-induced deformation. The resulting fragments are sieved to isolate particle size fractions between 50 and 300  $\mu\text{m}$ . All particles are irregularly shaped, white, and opaque, lacking distinctive surface features suitable for visual classification. The prepared microplastic fragments are stored in purified water for four weeks prior to imaging to minimize aggregation and sedimentation. Even after prolonged immersion, small air bubbles are frequently observed adhering to particle surfaces, indicating that gas entrapment at microplastic–water interfaces is a persistent phenomenon. These bubbles are not removed prior to imaging, as they represent realistic challenges encountered when handling hydrophobic microplastic particles in aqueous environments. (Joshua et al., 2025). In total, 600 particles are imaged and analyzed. For each of the three materials (PP, HDPE, and LDPE) 200 white particles in the size range from 50 - 300  $\mu\text{m}$  where used.

Figure 1 shows representative particles imaged with a Keyence microscope (VHX 7000). These particles are chosen specifically because they lack distinguishable visual features under standard illumination, making them difficult to classify by eye. This morphologically ambiguous appearance underscores the need for alternative optical approaches. Consequently, only polarization-sensitive imaging is applied in this study, and the resulting data is used to evaluate the performance of the classification framework.

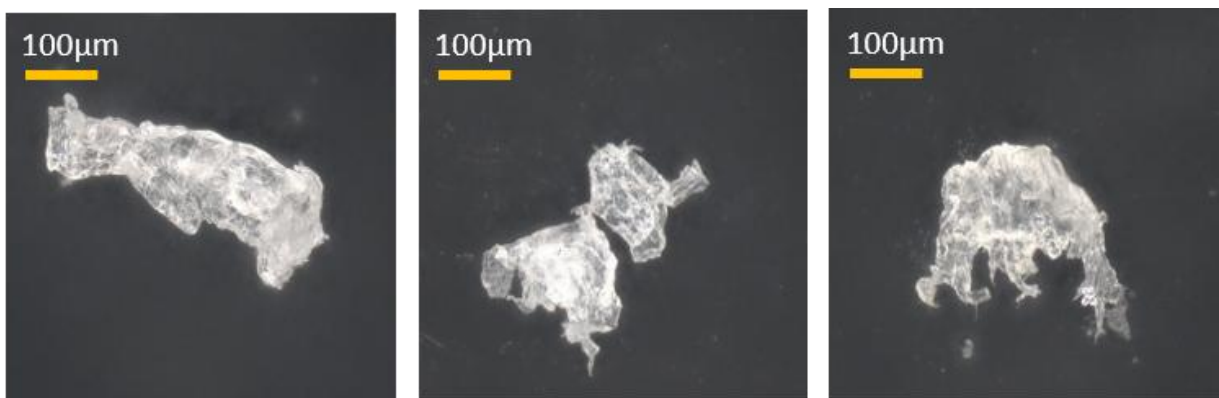


Figure 1: Example images of classified microplastic particles from left to right: PP, HDPE, and LDPE imaged under a Keyence digital microscope with ring light.

### 2.2. Optical setup and polarization imaging

The experimental setup is shown in Figure 2. Illumination is provided by a linearly polarized 532 nm diode laser (MD532-1-5(20x80), PicoTronics) operated at 1 mW. Beam focusing ensured a spot size of approximately 500  $\mu\text{m}$  in the sample plane (see Supplementary Information A for details on laser stability and beam divergence). Scattered light from the particles is collected at 120° relative to the incident beam, a geometry chosen to enhance material-dependent polarization contrast while reducing particle size scattering effects (Boss and Pegau, 2001; Twardowski et al., 2001).

Detection optics are mounted on an adjustable rail system to precisely control angle and working distance. Imaging is performed with a Krüss MSZ5000-T-S stereo zoom microscope equipped with 10 $\times$

wide-field eyepieces, a 0.7–4.5 $\times$  zoom objective, and a 2 $\times$  auxiliary lens, yielding a magnification range of 14 $\times$  to 90 $\times$ . At maximum zoom, the field of view corresponds to approximately 801  $\mu\text{m}$  with an effective pixel resolution of 0.39  $\mu\text{m}/\text{pixel}$ . A long-working-distance objective ensures clearance for the sample chamber while maintaining high-resolution focusing.

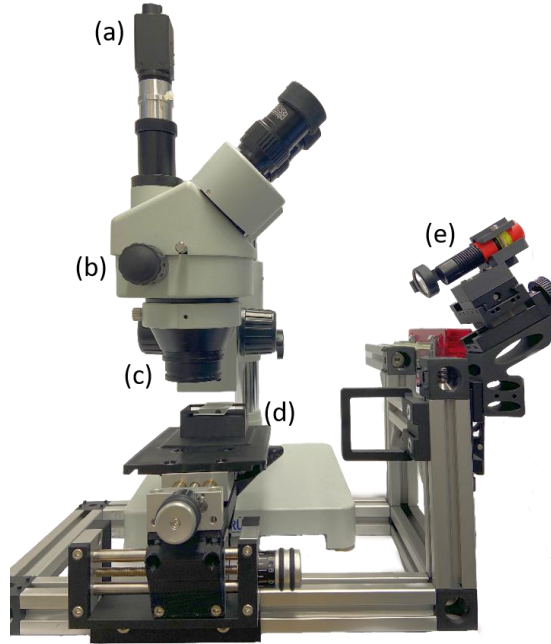


Figure 2: (a) Polarization camera, (b) adjustable magnification, (c) 2x objective, (d) precision stage and (e) Laser with focusing optics

A drop of the sample suspension is placed between, and enclosed by, two stacked microscope slides. The samples for analysis are fully immersed in water, with a reference distance of approximately 300  $\mu\text{m}$  derived from the largest particles on a single slide. Diffuse background illumination is provided by white light-emitting diode (LED) strips beneath a diffuser plate positioned 20 mm from the LEDs, ensuring homogeneous illumination across the sample plane.

Image acquisition is performed using the LUCID Vision Labs Triton™ TRI050S-QC polarization camera, which incorporates a Sony IMX250MYR CMOS sensor utilizing Sony's Polarsens Division-of-Focal-Plane (DoFP) technology. Raw polarization intensities at 0°, 45°, 90°, and 135° are captured with the LUCID Arena SDK (Software Development Kit). All automatic functions (auto-exposure, auto-gain, image enhancement) are disabled, and fixed exposure, gain, and white balance settings are used throughout all experiments. Focus is manually adjusted for each particle. Ambient temperature during measurements is 22–27 °C, and the setup is partially enclosed to suppress stray light. Because the excitation wavelength is 532 nm, only the green channel of the camera's bayer array is extracted for analysis, maximizing signal-to-noise ratio.

The native output of the DoFP polarization sensor consists of a pixel-level mosaic, where each pixel records intensity at only one of the four analyzer orientations. To reconstruct four full-resolution polarization images required for Stokes analysis, polarization demosaicing is performed. We applied Fourier-Domain Zero-Padding (FDZP) interpolation, a mathematically rigorous approach that aims to approximate the ideal continuous signal from discrete samples (Mihoubi et al., 2018; Qiu et al., 2021). This method preserves the integrity of polarization signals across the DoFP mosaic and provides a robust baseline for subsequent Stokes parameter estimation. Its known trade-off is the potential for

minor ringing artifacts near sharp edges. A detailed description of the interpolation algorithm is provided in Supplementary Information B.

The image processing workflow is summarized in Figure 3. From the reconstructed polarization images ( $I^0, I^{45}, I^{90}, I^{135}$ ), the linear Stokes parameters are computed as (Collett, 2005):

$$S_0 = I^0 + I^{90}, S_1 = I^0 - I^{90}, S_2 = I^{45} - I^{135}$$

From these, the two key polarization descriptors are derived:

$$\text{DOLP} = \frac{\sqrt{(S_1^2 + S_2^2)}}{S_0},$$

$$\text{AOLP} = \frac{1}{2} \times \arctan\left(\frac{S_2}{S_1}\right)$$

Only pixels with a nonzero value for  $S_0$  and  $S_1$  are evaluated, ensuring that DOLP and AOLP are computed exclusively in regions with measurable signal, and no division by zero error occurs. These descriptors capture polarization contrast independent of brightness or color and serve as the feature basis for classification (Collett, 2005).

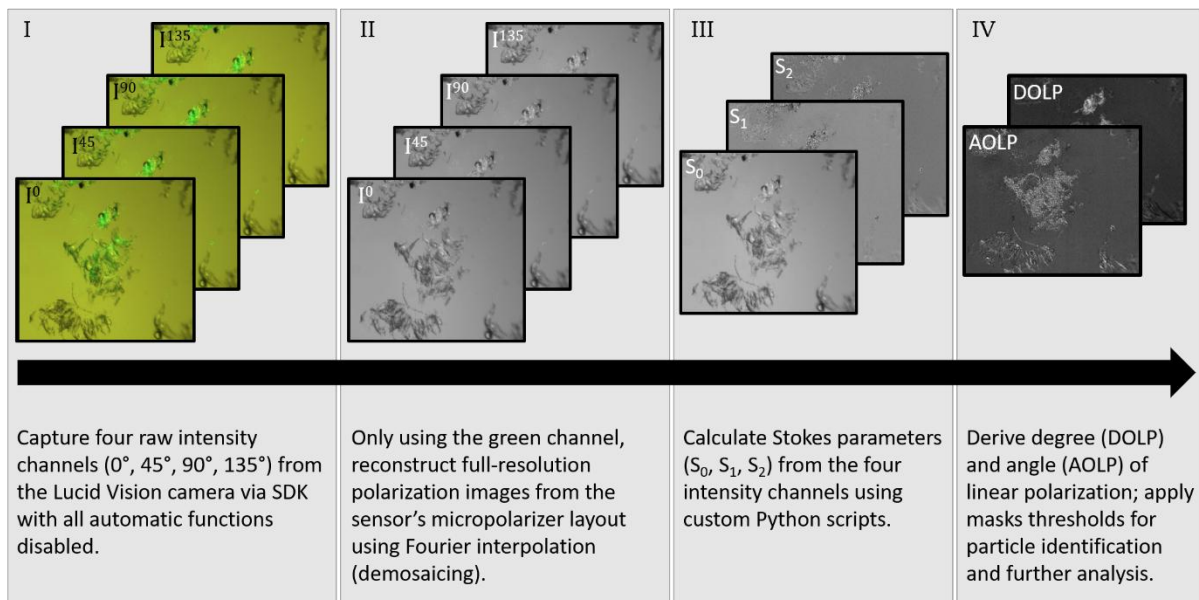


*Figure 3: Workflow for polarimetric image processing of microplastic particles using a Lucid Vision micropolarizer camera. I: Capture of four raw intensity channels ( $I^0, I^{45}, I^{90}, I^{135}$ ) using the camera's SDK with all automatic functions disabled. II: Reconstruction of full-resolution polarization images from the sensor's micropolarizer layout using only the green channel and applying Fourier interpolation (de-mosaicing). III: Calculation of the Stokes parameters ( $S_0, S_1, S_2$ ) from the four intensity channels using custom Python scripts. IV: Derivation of the final polarimetric images, including DOLP and AOLP, followed by mask threshold application for particle identification and further analysis.*

To prepare the data for machine learning, individual particles are segmented from the background using an automated image-processing pipeline (see Supplementary Information C). The workflow comprises grayscale conversion, denoising, local contrast enhancement, edge detection, and morphological refinement, resulting in filled binary masks of isolated particles. These masks are applied to the raw polarization images to restrict analysis to particle regions and suppress background artifacts.

### 2.3. Classification

To evaluate the robustness of the dataset and identify problematic particles in phase 1, a five-fold stratified cross-validation is performed. This evaluation is used to find images with errors that have a big negative impact on the classification training and evaluation accuracy. The images are only removed if they show great errors, such as being too small in size or air bubbles changing the polarization structure drastically. These removals are only done on the train and validation data, not on the test set, to not bloat up the classification results.

The dataset is split into five folds with preserved class distributions, so that a different 80/20 split for training and validation data is used in each iteration. This procedure is used to ensure that every particle image is evaluated in the validation set exactly once. Classification is carried out with a lightweight YOLO11n-based architecture (Ultralytics, 2023) initialized from pretrained weights. Hyperparameters are kept fixed across all folds (input size 640x640 pixel, batch size 32, 200 epochs, Adam optimizer). Only minor augmentations are used in the classification (see Supplementary Information D).

For each epoch, model predictions on the validation set are collected, and the per-image cross-entropy loss is computed as

$$L_i = -\log p(y_i | x_i)$$

where  $p(y_i | x_i)$  is the predicted probability of the true class. This metric enables the identification of particle images that consistently produce high classification error across multiple folds. Images with exceptionally high average or maximum loss are flagged as problematic samples. These typically corresponded to ambiguous, really small, and out-of-focus particles.

The cross-validation procedure serves two important purposes: First, it functions as a dataset quality control measure, checking for systematic errors, biases, or mislabeled samples within the dataset. Second, it allows for particle-level error analysis by identifying which microplastic fragments generate the greatest confusion for the classifier. Crucially, this initial phase is not intended to report final classification accuracy but rather to establish a reliable dataset foundation for subsequent training phases.

Phase 2 repeats the identical five-fold stratified cross-validation procedure executed in phase 1, but applies it to the based on the cleaned, refined dataset results from phase 1. This process serves to evaluate the influence of error images on the classification model and validate the effectiveness of the dataset refinement. The data partitions and all hyperparameters remain strictly fixed from phase 2. The validation set's purpose remained the monitoring of training progress via per-image cross-entropy loss calculation and the implementation of early stopping, which allowed for the objective selection of the single best-performing model instance for each feature set (AOLP and DOLP) from the five folds. The test Set remains completely untouched throughout this entire CV process. The subsequent evaluation methodology focuses on a final analysis using entirely unknown data. Following the selection of the best-performing model from the phase 2 cross-validation, two final, critical analyses are conducted on the 15% test set.

The first analysis is an unbiased performance estimation, where the selected model is evaluated only once on the test set. This provides an objective, final estimate of the classifier's generalization capability. The second analysis method is feature hierarchy quantification. This advanced analysis is also performed exclusively on the same untouched test set. The robustness of the final model is systematically assessed by evaluating the classification accuracy across five predefined feature degradation scenarios.

To determine the relative importance of distinct visual cues, specifically shape, structure, and texture, captured by the AOLP and DOLP feature sets, a systematic feature degradation study is performed. This analysis is executed by measuring the drop in classification accuracy relative to the baseline performance, which is established on the pristine original images (defined as shape + texture + context). Five distinct degradation scenarios are implemented to isolate the contribution of individual features. The structure & contour scenario involved replacing the particle's internal structure and texture with a uniform gray value, thereby isolating the contribution of the original, fine boundary shape. Conversely, the texture jitter test preserved the particle's overall shape and intensity histogram while destroying the local pixel arrangement by randomly shuffling pixel values within the particle's mask. To isolate the macro-shape, the Uniform Shape / Hull scenario aggressively smoothed the particle's complex, fine boundary and filled the resulting shape uniformly, leaving only the approximate macro-shape as a feature. Finally, the boundaries of performance are established using the Full Noise scenario, where the entire image (particle and background) is corrupted with random noise to define a lower performance limit.

### 3. Results

The model's classification performance is evaluated in two sequential phases: phase 1 establishes a baseline using five-fold stratified cross-validation on the original dataset, and phase 2 assesses performance post-refinement. The key performance metrics for all four validation runs are consolidated in Table 1, while the full fold-by-fold results are provided in the Supplementary Information E: Tables S1–S4. This culminates in a feature hierarchy quantification. The key performance metrics for all four validation runs are consolidated in Table 1.

#### 3.1. Feature Set Predictive Capacity

The AOLP feature set provides a stable material signature. The model achieves a high and consistent classification rate, evidenced by a mean maximum Top-1 Accuracy of  $0.85 \pm 0.03$  (Table 1). Generalization ability, assessed via the mean minimum validation loss, is stable at  $0.46 \pm 0.07$  across the folds, indicating a reliable fit to the validation data with only small variance. In contrast, the DOLP feature set demonstrates lower predictive capacity and increased performance variability (Table 1). The mean maximum accuracy is significantly lower at  $0.76 \pm 0.04$ , representing a 0.09-point decrease compared to the AOLP set. Furthermore, the mean minimum validation loss is markedly higher ( $0.65 \pm 0.06$ ), suggesting poorer model generalization and greater sensitivity to data partitioning.

The dataset refinement procedure, which involves the identification and removal of 30 problematic images (representing 6% of the total dataset) based on their consistently poor validation loss performance, is directly followed by a repeated five-fold stratified cross-validation. The subsequent significant and immediate performance improvements in both feature sets (AOLP and DOLP) demonstrate that these 30 images are substantial outliers that degrade the overall generalization capacity of the models. The model performance improves significantly on the refined dataset. The mean maximum Top-1 Accuracy increases to  $0.89 \pm 0.03$ , demonstrating a substantial gain in classification reliability. The DOLP feature set also exhibits stability improvement after data refinement, though its performance remained lower than AOLP. The mean maximum Top-1 Accuracy increased to  $0.81 \pm 0.03$ .

Table 1: Consolidated Summary of five-fold Cross-Validation Performance Across Phases

Phase	Feature Set	Mean Max Acc (Top1)	Mean Min Val Loss
1	AOLP	$0.85 \pm 0.03$	$0.46 \pm 0.07$
1	DOLP	$0.76 \pm 0.04$	$0.65 \pm 0.06$
2	AOLP	$0.89 \pm 0.03$	$0.31 \pm 0.09$
2	DOLP	$0.81 \pm 0.03$	$0.57 \pm 0.09$

The final predictive capability of the models is assessed on a held-out test dataset (untouched images), utilizing the best-performing fold identified during phase 2 cross-validation (AOLP: Fold 0, Max Acc: 0.92; DOLP: Fold 1, Max Acc: 0.85). For the test dataset with untouched images, the AOLP model attains a baseline test accuracy of 0.80, while the DOLP model achieves 0.79. The detailed classification error distributions for these top-performing models are visualized in the confusion matrices (see Figure 4).

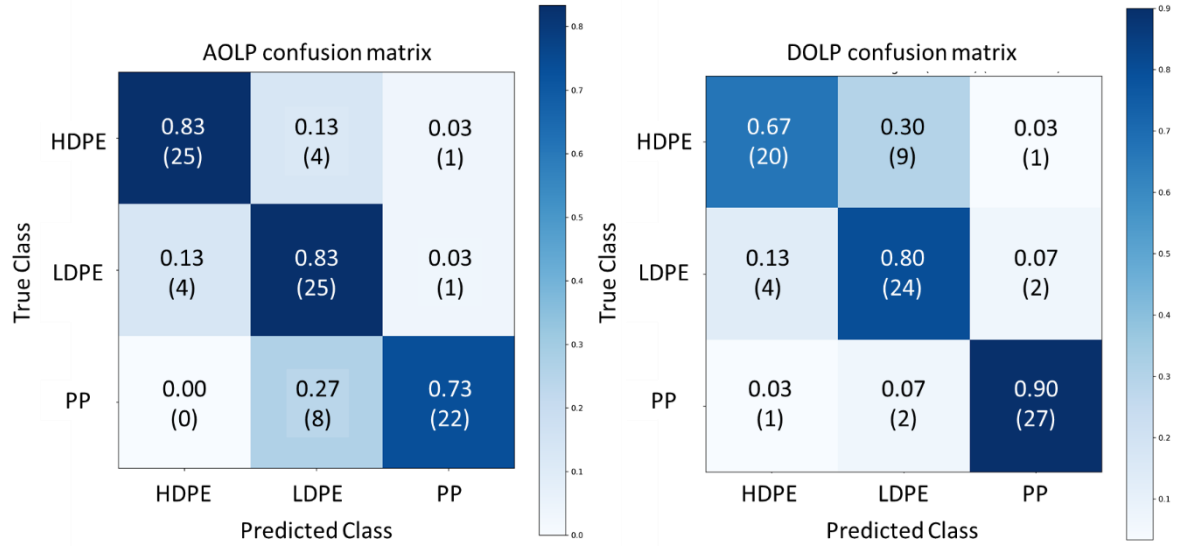


Figure 4: Normalized confusion matrices for the classification on the best performing folds for AOLP and DOLP

The AOLP model's main source of error is the misclassification of PP samples as LDPE, which accounted for 8 samples of the PP class errors. Additional confusion is observed between the two polyethylene variants: 4 samples of HDPE are misclassified as LDPE, and 4 samples of LDPE are misclassified as HDPE. In contrast, the DOLP confusion matrix indicates a significantly higher error rate for the HDPE class, with 9 samples being incorrectly predicted as LDPE. However, the DOLP model achieves the highest classification accuracy for the PP class, 0.90, compared to the 0.73 accuracy achieved by the AOLP model for the same material.

### 3.2. Feature Hierarchy Quantification: AOLP and DOLP

The feature hierarchy analysis is conducted on the single best-performing validation folds from phase 2 to quantify the relative importance of Shape (S), Texture (T), and Context (C) in the two feature signals. The results of this systematic feature degradation across five scenarios are summarized in Table 2 and Table 3 and visually presented in Figure 5 (AOLP) and Figure 6 (DOLP).

The analysis reveals distinct feature reliance patterns between the two models. The AOLP model demonstrates a primary reliance on the finer structured shape and inner texture of the particle. Removing the inner texture (Scenario 2) results in a 0.04 drop, which shows that removing the inner texture has a lower impact on the classification than corrupting the local texture arrangement (Scenario 3). However, removing all inner structural information and smoothing the boundary (Scenario 4: Uniform Shape) results in the largest single accuracy collapse to 0.38, confirming that the AOLP classification relies more on the fine-grained structured properties than on the general shape and size of the particle images. Conversely, the DOLP model shows even more critical dependence on the texture and inner structure. Degradation to a uniform internal structure (Scenario 2) causes a massive accuracy drop from 0.79 to 0.61. Further destruction of local texture (Scenario 3) further reduces the performance. The final removal of boundary detail (Scenario 4: Uniform Shape) has a smaller proportional effect than the initial structural corruption, suggesting the DOLP network prioritizes internal intensity patterns over exact shape.

Table 2: Feature Hierarchy Quantification via Feature Degradation Tests for the AOLP Signal.

Scenario	Accuracy	F1-Score (Macro)	Avg. Confidence
1. Original (S + T + C)	0.80	0.80	0.91
2. Structure & Contour (S + C)	0.76	0.75	0.83
3. Texture Jitter (S + T <sub>corrupted</sub> + C)	0.70	0.69	0.88
4. Uniform Shape (S <sub>smoothed</sub> )	0.38	0.36	0.77
5. Full Noise	0.36	0.21	0.98

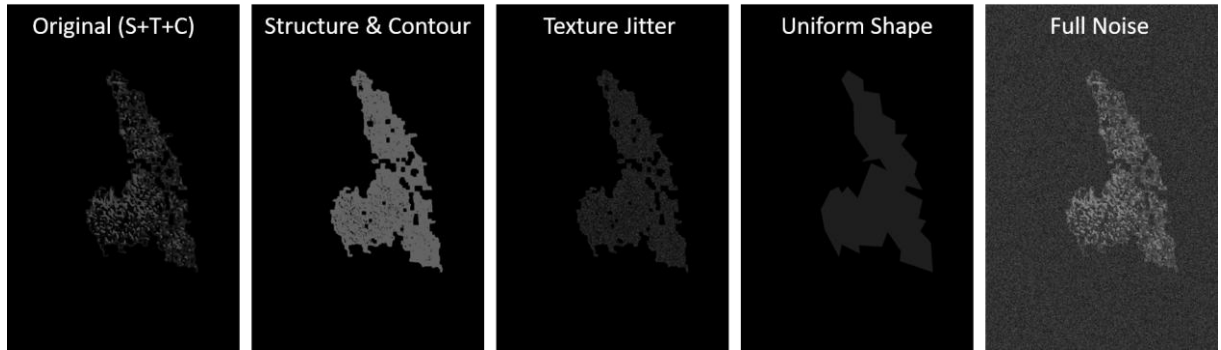


Figure 5: Feature-Degraded Image Scenarios for AOLP Classifier Robustness Assessment. It shows on a sample PP particle image the six degradation scenarios used to quantify the feature hierarchy (Shape, Texture, and Context) and test the robustness of the classifier.

The feature hierarchy analysis is similarly conducted on the single best-performing validation fold from phase 2 for the DOLP signal (Fold 1, Max Acc: 0.85), shown in Table 3, following the same feature degradation protocols.

Table 3: Feature Hierarchy Quantification via Feature Degradation Tests for the DOLP Signal.

Scenario	Accuracy	F1-Score (Macro)	Avg. Confidence
1. Original (S + T + C)	0.79	0.79	0.88
2. Structure & Contour (S + C)	0.61	0.61	0.78
3. Texture Jitter (S + T <sub>corrupted</sub> + C)	0.51	0.48	0.84
4. Uniform Shape (S <sub>smoothed</sub> )	0.39	0.35	0.78
5. Full Noise	0.33	0.17	0.97

The baseline accuracy for the uncorrupted DOLP image (Test 1: S+T+C) is 0.79. The feature degraded images are shown in Figure 6.

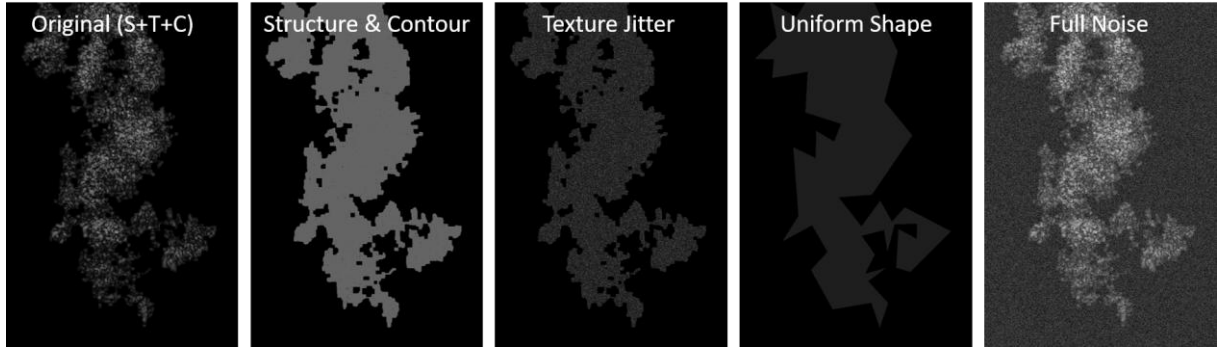


Figure 6: Feature-Degraded Image Scenarios for DOLP Classifier Robustness Assessment. Shows on a sample PP particle image the six degradation scenarios used to quantify the feature hierarchy (Shape, Texture, and Context) and test the robustness of the classifier.

## 4. Discussion

### 4.1. Impact of Data Refinement and Feature Set Stability

The classification performance clearly establishes the superior predictive capacity and inherent stability of the AOLP feature set compared to DOLP. Across all phases, AOLP consistently demonstrated higher classification accuracy (up to 0.92 in phase 2, Table 2) alongside lower performance variance across folds. This 8-percentage-point margin in maximum accuracy in the validation indicates that the AOLP signal encapsulates a more robust intrinsic material signature, likely related to its angle of polarized light, that is inherently less susceptible to measurement artifacts and environmental variables than the DOLP measurement.

The necessity of the two-phase approach is fully justified by the results. The pronounced variability observed in the phase 1 cross-validation results (detailed in Supplementary Information E: Tables S1 and S2) signals significant dataset heterogeneity and potential label noise. This initial analysis reveals that the model is prematurely overfitting to easily classifiable subsets, failing to generalize to more ambiguous or unrepresented samples. The subsequent stability and convergence achieved in phase 2, evidenced by the higher mean accuracy and reduced standard deviation, confirm that systematic dataset cleaning is a critical prerequisite for achieving stable deep learning classification in microplastic analysis. The model instances selected for the deeper analysis represent the highest-quality models achieved on the refined dataset.

#### 4.2. Comparative Feature Importance Hierarchy (AOLP vs. DOLP)

The feature hierarchy analysis (Section 3.2) provides a quantitative, mechanistic understanding of the CNN's decision-making process for both polarization features, confirming a core dependency on internal structural integrity while simultaneously revealing specific, critical vulnerabilities for the DOLP signal. For both polarization signals, the destruction of the unique internal texture and finer shape (Test 5: uniform shape, Table 2 and Table 3) results in the largest functional drop in accuracy:  $\Delta\text{AOLP} = -0.42$ ;  $\Delta\text{DOLP} = -0.40$ . This is the most significant finding: the deep learning model is primarily classifying microplastics not based on their external contour(shape), but on the learned pattern of the image's internal structural properties. The model effectively uses the texture and structure, particularly in the AOLP signal, as a proxy for the material's unique class characteristics. This reliance on structure is a highly desirable characteristic, as it ties the classification directly to fundamental polymer morphology rather than external appearance. The fact that the accuracy plummets to near-random chance (0.35 – 0.41) when this inner structure is removed suggests that the model is performing a texture-based, sub-pixel analysis rather than a traditional shape-recognition task.

A critical functional distinction between the two feature sets is revealed in their differential response to feature degradation, strongly supporting the conclusion that DOLP is less robust as a feature for this task. This lower robustness is evident in two ways. First, the model shows reduced tolerance to local texture rearrangement in DOLP ( $\Delta\text{DOLP} = 0.10$  from Scenario 2 to 3) compared to AOLP ( $\Delta\text{AOLP} = -0.06$  from Scenario 2 to 3). This indicates a higher functional fragility for the DOLP feature set, suggesting that the local, fine-scale arrangement of the DOLP signal is more easily corrupted by position-based noise. Physically, DOLP is strongly influenced by microscopic surface roughness, and scrambling these local features disrupts the predictive pattern more severely than it does for the more spatially coherent AOLP signal, where the overall pattern holds greater weight in classification. Second, the role of external shape demonstrates that while the internal texture is most crucial, the model efficiently utilizes the full extent of the particle outline information but does not rely purely on the overall macro-shape. The moderate performance in the structure & contour test (Scenario 2) for both AOLP (accuracy = 0.76) and DOLP (accuracy 0.61) confirms this. However, the accuracy drop is significantly larger for DOLP ( $\Delta\text{Delta} = -0.18$ ) than for AOLP ( $\Delta\text{AOLP} = -0.04$ ), comparing the original image (Scenario 1) to the structure & contour image (Scenario 2). This highlights that the AOLP network is far better at compensating for missing textural information using its remaining shape features, whereas the DOLP network is immediately and critically impacted by the loss of internal texture.

A final, critical functional distinction lies in the models' class-specific predictive strengths, as shown in the confusion matrices (Figure 4). The AOLP model excels at distinguishing between the two polyethylene variants (HDPE and LDPE), exhibiting a high true positive rate for both classes (0.83 each) and a low misclassification rate between them. However, it struggles with PP, misclassifying 27% of PP samples as LDPE. Conversely, the DOLP model demonstrates superior performance in isolating the PP class (0.90 true positive rate) but exhibits a much higher confusion between the polyethylenes, misclassifying 30% of HDPE as LDPE. This complementary nature of the two signals suggests that an ensemble model combining the AOLP and DOLP feature sets would leverage the strengths of each, likely achieving a more accurate and robust overall classification across all three polymer types than either signal can achieve alone.

## 5. Conclusion

The dual-phase methodology employed in this study confirmed the superior performance and stability of the AOLP signal as a robust feature set for microplastic classification, achieving a peak mean accuracy of 80% on the test dataset. This project makes a critical contribution by demonstrating that deep learning, utilizing only reflected light polarization, is effective for material classification in this specific application, offering a promising alternative to more expensive or complex spectroscopic methods. The study also demonstrates the necessity of dataset refinement as a critical prerequisite for achieving stable model performance, significantly reducing heterogeneity and improving generalization capability.

Most notably, the feature hierarchy analysis provides a mechanistic understanding of the CNN's decision-making process, proving that classification is overwhelmingly driven by the micro-structural integrity and internal texture of the particle image, rather than its macro-shape. Crucially, the successful classification of particles submerged in water establishes the method's potential for direct application in high-throughput, flow-through analytical systems. Specifically, the destruction of the particle image's internal structure led to the most drastic reduction in accuracy for both AOLP ( $\Delta$ AOLP = -0.42) and DOLP ( $\Delta$ DOLP = -0.40). This functional finding provides a strong foundation for future physics-informed AI development in this field by directing research attention toward micro-structural features that encode fundamental material characteristics, rather than external shape. The comparison between the two signals revealed two key differences. First, the AOLP signal proves to be significantly more robust, particularly in its resilience to the loss of textural information, as evidenced by its minimal accuracy drop ( $\Delta$ AOLP = -0.04) when internal texture is removed while the particle outline remains. Second, the signals exhibited complementary class distinguishability: the AOLP model excels at separating polyethylenes (HDPE and LDPE), while the DOLP model is superior at isolating PP. We acknowledge that our mechanical preparation method may induce internal stresses that differ from those in environmentally weathered secondary microplastics. Future work should validate this method on environmental samples to ensure the learned features are generalizable.

Finally, the analysis strongly suggests that while AOLP is the more robust singular feature, the most advanced solution lies in multimodal classification. A feature fusion approach would allow the classifier to leverage the inherent stability of the AOLP signal (which encodes the fundamental material type via its angle of polarization) alongside the high-sensitivity surface and contextual data provided by the DOLP signal (which encodes surface roughness, scattering, and context heterogeneity). This combined optical signature promises a more complete, resilient, and highly informative classification system for automated microplastic analysis.

## Acknowledgments

This work was supported by the Helmholtz Association under the *Helmholtz Imaging Call 2025* (ZT-I-PF-4-079, PlastoView).

Declaration of generative AI and AI-assisted technologies in the manuscript preparation process

During the preparation of this work, the authors used AI tools to improve clarity and fluency in the writing process. After using these tools, the authors reviewed and edited the content as needed and take full responsibility for the content of the published article.

## References

Al Alwan, B., Ismail, B., El Jery, A., Badawi, A.K., 2024. State-of-the-art strategies for microplastics mitigation in aquatic environments: Identification, technological innovations, and prospects for advancement. *J. Water Process Eng.* 61, 105336. <https://doi.org/10.1016/j.jwpe.2024.105336>

Araujo, C.F., Nolasco, M.M., Ribeiro, A.M.P., Ribeiro-Claro, P.J.A., 2018. Identification of microplastics using Raman spectroscopy: Latest developments and future prospects. *Water Res.* 142, 426–440. <https://doi.org/10.1016/j.watres.2018.05.060>

Avio, C.G., Gorbi, S., Regoli, F., 2017. Plastics and microplastics in the oceans: From emerging pollutants to emerged threat. *Mar. Environ. Res.* 128, 2–11. <https://doi.org/10.1016/j.marenvres.2016.05.012>

Beck, A.J., Kaandorp, M., Hamm, T., Bogner, B., Kossel, E., Lenz, M., Haeckel, M., Achterberg, E.P., 2023. Rapid shipboard measurement of net-collected marine microplastic polymer types using near-infrared hyperspectral imaging. *Anal. Bioanal. Chem.* 415, 2989–2998. <https://doi.org/10.1007/s00216-023-04634-6>

Boss, E., Pegau, W.S., 2001. Relationship of light scattering at an angle in the backward direction to the backscattering coefficient. *Appl. Opt.* 40, 5503. <https://doi.org/10.1364/AO.40.005503>

Collett, E., 2005. Field Guide to Polarization. SPIE. <https://doi.org/10.1117/3.626141>

Enfrin, M., Hachemi, C., Hodgson, P.D., Jegatheesan, V., Vrouwenvelder, J., Callahan, D.L., Lee, J., Dumée, L.F., 2021. Nano/micro plastics – Challenges on quantification and remediation: A review. *J. Water Process Eng.* 42, 102128. <https://doi.org/10.1016/j.jwpe.2021.102128>

Fischer, M., Scholz-Böttcher, B.M., 2019. Microplastics analysis in environmental samples – recent pyrolysis-gas chromatography-mass spectrometry method improvements to increase the reliability of mass-related data. *Anal. Methods* 11, 2489–2497. <https://doi.org/10.1039/C9AY00600A>

Huang, J., Zhu, Y., Li, Y., Lam, E.Y., 2023. Snapshot Polarization-Sensitive Holography for Detecting Microplastics in Turbid Water. *ACS Photonics* 10, 4483–4493. <https://doi.org/10.1021/acsphotonics.3c01350>

Jahnke, A., Arp, H.P.H., Escher, B.I., Gewert, B., Gorokhova, E., Kühnel, D., Ogonowski, M., Potthoff, A., Rummel, C., Schmitt-Jansen, M., Toorman, E., MacLeod, M., 2017. Reducing Uncertainty and Confronting Ignorance about the Possible Impacts of Weathering Plastic in the Marine Environment. *Environ. Sci. Technol. Lett.* 4, 85–90. <https://doi.org/10.1021/acs.estlett.7b00008>

Jones, R.R., Hooper, D.C., Zhang, L., Wolverton, D., Valev, V.K., 2019. Raman Techniques: Fundamentals and Frontiers. *Nanoscale Res. Lett.* 14, 231. <https://doi.org/10.1186/s11671-019-3039-2>

Joshua, A.M., Aznir, P.A.D., Lau, E.V., 2025. Understanding microplastic flotation through microbubble-microplastic interactions. *Surf. Interfaces* 64, 106399. <https://doi.org/10.1016/j.surfin.2025.106399>

Koestner, D., Foster, R., El-Habashi, A., Cheatham, S., 2024. Measurements of the inherent optical properties of aqueous suspensions of microplastics. *Limnol. Oceanogr. Lett.* 9, 487–497. <https://doi.org/10.1002/lol2.10387>

Koestner, D., University of Bergen, Foster, R., El-Habashi, A., 2023. On the Potential for Optical Detection of Microplastics in the Ocean. *Oceanography*. <https://doi.org/10.5670/oceanog.2023.s1.15>

Kotar, S., McNeish, R., Murphy-Hagan, C., Renick, V., Lee, C.-F.T., Steele, C., Lusher, A., Moore, C., Minor, E., Schroeder, J., Helm, P., Rickabaugh, K., De Frond, H., Gesulga, K., Lao, W., Munno, K., Thornton Hampton, L.M., Weisberg, S.B., Wong, C.S., Amarpuri, G., Andrews, R.C., Barnett, S.M., Christiansen, S., Cowger, W., Crampond, K., Du, F., Gray, A.B., Hankett, J., Ho,

K., Jaeger, J., Lilley, C., Mai, L., Mina, O., Lee, E., Primpke, S., Singh, S., Skovly, J., Slifko, T., Sukumaran, S., Van Bavel, B., Van Brocklin, J., Vollnhals, F., Wu, C., Rochman, C.M., 2022. Quantitative assessment of visual microscopy as a tool for microplastic research: Recommendations for improving methods and reporting. *Chemosphere* 308, 136449. <https://doi.org/10.1016/j.chemosphere.2022.136449>

Liu, T., Yu, S., Zhu, X., Liao, R., Zhuo, Z., He, Y., Ma, H., 2021. In-situ Detection Method for Microplastics in Water by Polarized Light Scattering. *Front. Mar. Sci.* 8, 739683. <https://doi.org/10.3389/fmars.2021.739683>

Lusher, A.L., Bråte, I.L.N., Munno, K., Hurley, R.R., Welden, N.A., 2020. Is It or Isn't It: The Importance of Visual Classification in Microplastic Characterization. *Appl. Spectrosc.* 74, 1139–1153. <https://doi.org/10.1177/0003702820930733>

Mihoubi, S., Lapray, P.-J., Bigué, L., 2018. Survey of Demosaicking Methods for Polarization Filter Array Images. *Sensors* 18, 3688. <https://doi.org/10.3390/s18113688>

Mutuku, J., Yanotti, M., Tocock, M., Hatton MacDonald, D., 2024. The Abundance of Microplastics in the World's Oceans: A Systematic Review. *Oceans* 5, 398–428. <https://doi.org/10.3390/oceans5030024>

Pivokonsky, M., Cermakova, L., Novotna, K., Peer, P., Cajthaml, T., Janda, V., 2018. Occurrence of microplastics in raw and treated drinking water. *Sci. Total Environ.* 643, 1644–1651. <https://doi.org/10.1016/j.scitotenv.2018.08.102>

Qiu, S., Fu, Q., Wang, C., Heidrich, W., 2021. Linear Polarization Demosaicking for Monochrome and Colour Polarization Focal Plane Arrays. *Comput. Graph. Forum* 40, 77–89. <https://doi.org/10.1111/cgf.14204>

Rahman, A., Sarkar, A., Yadav, O.P., Achari, G., Slobodnik, J., 2021. Potential human health risks due to environmental exposure to nano- and microplastics and knowledge gaps: A scoping review. *Sci. Total Environ.* 757, 143872. <https://doi.org/10.1016/j.scitotenv.2020.143872>

Rauert, C., Charlton, N., Bagley, A., Dunlop, S.A., Symeonides, C., Thomas, K.V., 2025. Assessing the Efficacy of Pyrolysis–Gas Chromatography–Mass Spectrometry for Nanoplastic and Microplastic Analysis in Human Blood. *Environ. Sci. Technol.* 59, 1984–1994. <https://doi.org/10.1021/acs.est.4c12599>

Schymanski, D., Oßmann, B.E., Benismail, N., Boukerma, K., Dallmann, G., Von Der Esch, E., Fischer, D., Fischer, F., Gilliland, D., Glas, K., Hofmann, T., Käppler, A., Lacorte, S., Marco, J., Rakwe, M.E., Weisser, J., Witzig, C., Zumbülte, N., Ivleva, N.P., 2021. Analysis of microplastics in drinking water and other clean water samples with micro-Raman and micro-infrared spectroscopy: minimum requirements and best practice guidelines. *Anal. Bioanal. Chem.* 413, 5969–5994. <https://doi.org/10.1007/s00216-021-03498-y>

Sesay, R.E.V., Azizi, M.I., Rahmani, B., Rajendra, P., 2024. Advancing Micro Plastic Analysis: A Comprehensive Review of Detection and Characterization Techniques. *Asian J. Environ. Ecol.* 23, 85–102. <https://doi.org/10.9734/ajee/2024/v23i12636>

Sharma, S., Chatterjee, S., 2017. Microplastic pollution, a threat to marine ecosystem and human health: a short review. *Environ. Sci. Pollut. Res.* 24, 21530–21547. <https://doi.org/10.1007/s11356-017-9910-8>

Shim, W.J., Hong, S.H., Eo, S.E., 2017. Identification methods in microplastic analysis: a review. *Anal. Methods* 9, 1384–1391. <https://doi.org/10.1039/C6AY02558G>

Twardowski, M.S., Boss, E., Macdonald, J.B., Pegau, W.S., Barnard, A.H., Zaneveld, J.R.V., 2001. A model for estimating bulk refractive index from the optical backscattering ratio and the implications for understanding particle composition in case I and case II waters. *J. Geophys. Res. Oceans* 106, 14129–14142. <https://doi.org/10.1029/2000JC000404>

Veerasingam, S., Ranjani, M., Venkatachalamapathy, R., Bagaev, A., Mukhanov, V., Litvinyuk, D., Mugilarasan, M., Gurumoorthi, K., Guganathan, L., Aboobacker, V.M., Vethamony, P., 2021. Contributions of Fourier transform infrared spectroscopy in microplastic pollution research: A review. *Crit. Rev. Environ. Sci. Technol.* 51, 2681–2743. <https://doi.org/10.1080/10643389.2020.1807450>

Winiarska, E., Jutel, M., Zemelka-Wiacek, M., 2024. The potential impact of nano- and microplastics on human health: Understanding human health risks. Environ. Res. 251, 118535.

<https://doi.org/10.1016/j.envres.2024.118535>

Zhu, Y., Li, Y., Huang, J., Lam, E.Y., 2024. Smart polarization and spectroscopic holography for real-time microplastics identification. Commun. Eng. 3, 32. <https://doi.org/10.1038/s44172-024-00178-4>

# Supplementary Information: Classification of Microplastic Particles in Water using Polarized Light Scattering and Machine Learning Methods

## A. Laser stability and beam divergence

Prior to the measurements, the output power of the 532 nm diode laser (MD532-1-5(20x80), PicoTronics) was assessed for temporal stability. Measurements were performed using a calibrated optical power meter (Model: [LaserChecker™/COHERENT]), both directly at the laser exit and at the sample position. After a 15-minute warm-up phase, the laser output stabilized at 1 mW (SD <0.01 mW). Stability was monitored over a 2-hour period at 10-minute intervals under ambient laboratory conditions (22–27 °C). The observed variance remained below 1 %, with no significant fluctuations detected. The diode laser is specified with a beam divergence of 0.5 mrad; in the setup, the beam was focused through a collimating lens to ensure uniform illumination of the particle field of view.

## B. Polarization de-mosaicing via Fourier-Domain Interpolation

The Division-of-Focal-Plane (DoFP) sensor arrangement results in four spatially sub-sampled intensity images,  $I_\theta(x,y)$ , where  $\theta \in \{0^\circ, 45^\circ, 90^\circ, 135^\circ\}$ . Each image  $I_\theta$  has a spatial resolution of  $H/2 \times W/2$  and contains only the directly measured pixels, with no zero-padding applied (as confirmed by the sensor configuration). The objective of demosaicing is to reconstruct the four full-resolution ( $H \times W$ ) intensity images,  $I_\theta'$ .

Our method employs Fourier-domain zero-padding (FDZP), which achieves sinc-interpolation—the theoretically ideal reconstruction function for band-limited signals (Eskreis-Winkler et al., 2017). The process for each sub-sampled polarisation channel  $I_\theta$  is as follows:

1. Fourier Transform: The image is transformed into the frequency domain:

$$F_\theta(u, v) = F\{I_\theta(x, y)\}$$

2. Zero-Padding (up-sampling): The low-resolution frequency spectrum  $F_\theta$  is embedded into a higher-resolution grid (size  $H \times W$ ) by padding the high-frequency quadrants with zeros. This process retains the integrity of the sampled low-frequency information while defining the high-frequency components as zero, consistent with the ideal sinc function reconstruction:

$$F_\theta'(u, v) = \text{Zero} - \text{Pad}\{F_\theta(u, v)\}$$

3. Inverse Fourier transform: The full-resolution image is obtained by the inverse transform:

$$I_\theta'(x, y) = F^{-1}\{F_\theta'(u, v)\}$$

This FDZP approach effectively performs a nearest-neighbor interpolation in the frequency domain, resulting in sinc interpolation in the spatial domain. A known consequence of this theoretically ideal interpolation is the introduction of Gibbs ringing artifacts at sharp material or polarisation boundaries in the final images, a factor that is generally less critical in the analysis of water bodies compared to high-detail terrestrial scenes (Mihoubi et al., 2018; Qiu et al., 2021). The resulting  $I_\theta'$  are then used to calculate the Stokes parameters.

## C. Image preprocessing and particle segmentation

Raw polarization-resolved intensity images were exported directly from the Lucid Vision SDK. All internal auto-functions (white balance, auto-exposure, auto-gain) were disabled.

The segmentation workflow proceeded as follows:

1. Preprocessing:
  - a. Conversion to grayscale.
  - b. Non-local means filtering to reduce high-frequency noise while preserving edge information.
  - c. Local contrast enhancement using CLAHE (clip limit = [2.0]).
2. Edge detection:
  - a. Canny edge detector with low/high thresholds = 30/100.
3. Morphological refinement:
  - a. Closing to connect fragmented edges.
  - b. Dilation to reinforce particle boundaries.
  - c. A second closing step to ensure filled masks.
4. Connected-component analysis:
  - a. Largest connected component retained.
  - b. Resulting binary mask applied to the original grayscale image.

This pipeline produced consistent particle-only masks with background suppression across all samples.

## D. Classification details

For classification, DOLP and AOLP images were treated as separate input channels. Training was conducted using the YOLOv11-nano cls architecture (Ultralytics, 2023).

- Dataset split: 70% train, 15% validation, 15% test. Particles were uniquely assigned to one split to avoid leakage.
- Labels: Ground-truth labels derived from source-verified single-material samples embedded in distilled water.
- Training setup:
  - Input resolution: 640×640 px.
  - Epochs: 200.
  - Early stopping: 50
  - Batch size: 32.
  - Optimizer: Adam.
  - Initialization: ImageNet pretraining.
  - Data augmentation: Erasing and minor intensity changes
- Evaluation: Performance metrics included top-1 accuracy, class-specific confidence scores, and confusion matrices.
- Runtime environment: Training performed on a local workstation with PyTorch and the Ultralytics API. Logs, models, and predictions were archived for reproducibility.

## E. Results of five-fold stratified cross-validation on original dataset:

Table S1: AOLP Phase 1 K-fold cross-validation results

Fold	Epoch (Min Val Loss)	Min Val Loss	Train Loss (at Min Val Loss)	Acc. (at Min Val Loss)	Epoch (Max Acc)	Max Acc (Top1)
0	72	0.36	0.22	0.88	73	0.90
1	22	0.54	0.41	0.79	32	0.83
2	38	0.50	0.42	0.78	70	0.84
3	41	0.47	0.35	0.79	48	0.84
4	127	0.41	0.16	0.81	77	0.83
Mean $\pm$ Std Dev	N/A	$0.46 \pm 0.07$	$0.31 \pm 0.12$	$0.81 \pm 0.04$	N/A	$0.85 \pm 0.03$

Table S2: DOLP Phase 1 K-fold cross-validation results

Fold	Epoch (Min Val Loss)	Min Val Loss	Train Loss (at Min Val Loss)	Acc. (at Min Val Loss)	Epoch (Max Acc)	Max Acc (Top1)
0	55	0.63	0.45	0.74	43	0.76
1	27	0.75	0.67	0.66	71	0.69
2	24	0.63	0.62	0.72	94	0.80
3	30	0.61	0.67	0.75	29	0.79
4	27	0.61	0.67	0.73	67	0.77
Mean $\pm$ Std Dev	N/A	$0.65 \pm 0.06$	$0.62 \pm 0.10$	$0.72 \pm 0.04$	N/A	$0.76 \pm 0.04$

Cleaned dataset:

Table S3: AOLP Phase 2 K-fold cross-validation results

Fold	Epoch (Min Val Loss)	Min Val Loss	Train Loss (at Min Val Loss)	Acc. (at Min Val Loss)	Epoch (Max Acc)	Max Acc (Top1)
0	93	0.24	0.31	0.91	92	0.92
1	81	0.42	0.20	0.85	81	0.85
2	40	0.33	0.41	0.85	17	0.88
3	87	0.35	0.19	0.88	71	0.88
4	36	0.19	0.37	0.88	33	0.92
Mean $\pm$ Std Dev	N/A	$0.31 \pm 0.09$	$0.30 \pm 0.10$	$0.87 \pm 0.02$	N/A	$0.89 \pm 0.03$

Table S4: DOLP Phase 2 K-fold cross-validation n results

Fold	Epoch (Min Val Loss)	Min Val Loss	Train Loss (at Min Val Loss)	Acc. (at Min Val Loss)	Epoch (Max Acc)	Max Acc (Top1)
0	23	0.61	0.71	0.74	25	0.78
1	123	0.46	0.34	0.82	83	0.85
2	74	0.66	0.33	0.74	64	0.78
3	61	0.65	0.41	0.75	50	0.79
4	126	0.49	0.37	0.81	127	0.83
Mean $\pm$ Std Dev	N/A	$0.57 \pm 0.09$	$0.43 \pm 0.16$	$0.77 \pm 0.04$	N/A	$0.81 \pm 0.03$